ACS OMEGA

Open Access

http://pubs.acs.org/journal/acsodf

Article

Addressing Irreversibility and Structural Distortion in WS_2 Inorganic Fullerene-Like Nanoparticles: Effects of Voltage Cutoff Experiments in Beyond Li^+-Ion Storage Applications

Sonjoy Dey,* Arijit Roy, Shakir Bin Mujib, Manjunath Krishnappa, Alla Zak, and Gurpreet Singh*

Cite This: *ACS Omega* 2024, 9, 17125−17136

Read Online

ACCESS | Metrics & More | Article Recommendations | Supporting Information

ABSTRACT: Large interlayer spacing beneficially allows Na^+- and K^+-ion storage in transition-metal dichalcogenide (TMD)-based electrodes, but side reactions and volume change, which pulverize the TMD crystalline structure, are persistent challenges for the utilization of these materials in next-generation devices. This study first determines whether irreversibility due to structural distortion, which results in poor cycling stability, is also apparent in the case of inorganic fullerene-like (IF) tungsten disulfide (WS_2) nanocages (WS_2IF). To address these problems, this study proposes upper and lower voltage cutoff experiments to limit specific reactions in Na^+/WS_2IF and K^+/WS_2IF half-cells. Three-dimensional (3D) differential capacity curves and derived surface plots highlight the continuation of reversible reactions when a high upper cutoff technique is applied, thereby indirectly suggesting restricted structural dissolution. This resulted in improved capacity retention with stable performance and a higher Coulombic efficiency, laying the ground for the use of TMD-based materials beyond Li^+-ion storage devices.

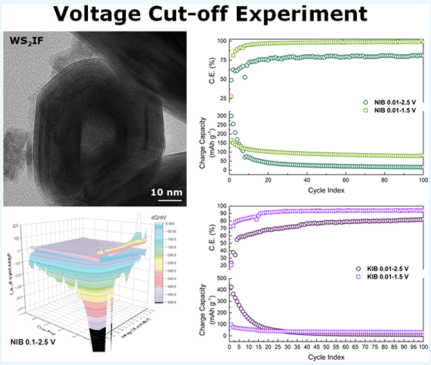

INTRODUCTION

In 1985, the discovery of a highly symmetrical and stable C_{60}−fullerene hollow nanostructure[1] inaugurated a new paragon in chemistry. Much like C_{60}, layered compounds of TMDs, generally known as MX_2, where M represents a transition metal hexagonally packed with two X or chalcogen atoms, can also form hollow cage-like structures using hexagons and triangles and/or rhombi arranged as symmetric tetrahedron or octahedron.[1] Research initiatives by Tenne et al. have driven the extensive scalability[2] of such zero-dimensional (0D) nanoparticles for various fields: light−matter interactions, bulk electrical transport,[3] solid lubricants,[4] biomarkers, drug delivery vehicles, coatings for orthodontic wires, and endodontic files.[5] Although the efficacy of nanomaterials cannot be disregarded, the current literature fails to explore the electrochemical properties of IF nanophase materials. In general, nanomaterials (e.g., layered oxides, nano hard carbon, etc.) present a mechanical advantage over traditional materials mainly due to their reduced size.[6−10] Nanomaterials or nanostructured electrodes can accomodate large strains without pulverization as the particle size is equal to or below the typical crack size during charge storage.[11]

Many studies have focused on distinct WS_2 structures with a wide dimensional variety for use in rechargeable secondary alkali-metal-ion batteries, especially Li^+-ion storage behavior inside WS_2 nanostructures, including nanosheets,[12] nano-honeycombs,[13] nanoflowers,[13] nanotubes,[14] and onion-like structures.[15] However, investigation regarding electrochemical charge storage of earth-abundant alkali-metal ions, such as Na^+ and K^+ ions, is rarely found in the existing literature, especially for WS_2IF structures. Previous investigations have highlighted the existing drawbacks of WS_2, namely, low electronic conductivity, high molecular weight, nanosheet reaggregation phenomena, chalcogen species dissolution, and extreme volume change. These are more apparent during reversible Na^+- and K^+-ion storage, because Na^+ and K^+ ions are bulkier in size compared to Li-ions and present slower diffusion kinetics.[16,17] Usual strategies to curb the inherent deficiencies of TMD-based electrodes include hybrid structure formation with carbon or rhenium[18] additives to provide required conductivity to the nanofillers,[19] enhancement of interlayer spacing,[20] and the induction of regional disorder[21] to facilitate higher alkali-metal-ion storage sites. Nevertheless, such strategies require convoluted synthesis parameters, instigate impurities within the crystal, and decrease the cell's overall performance. Therefore, to enable the practical application of TMD nanostructures beyond Li^+-ion batteries, alternative engineering strategies are necessary.

This investigation applied upper and lower voltage cutoff techniques to achieve efficient and reversible electrochemical storage beyond Li^+ ions in 0D WS_2IF structures as a

Received: December 6, 2023
Revised: March 10, 2024
Accepted: March 14, 2024
Published: April 1, 2024

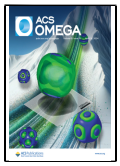

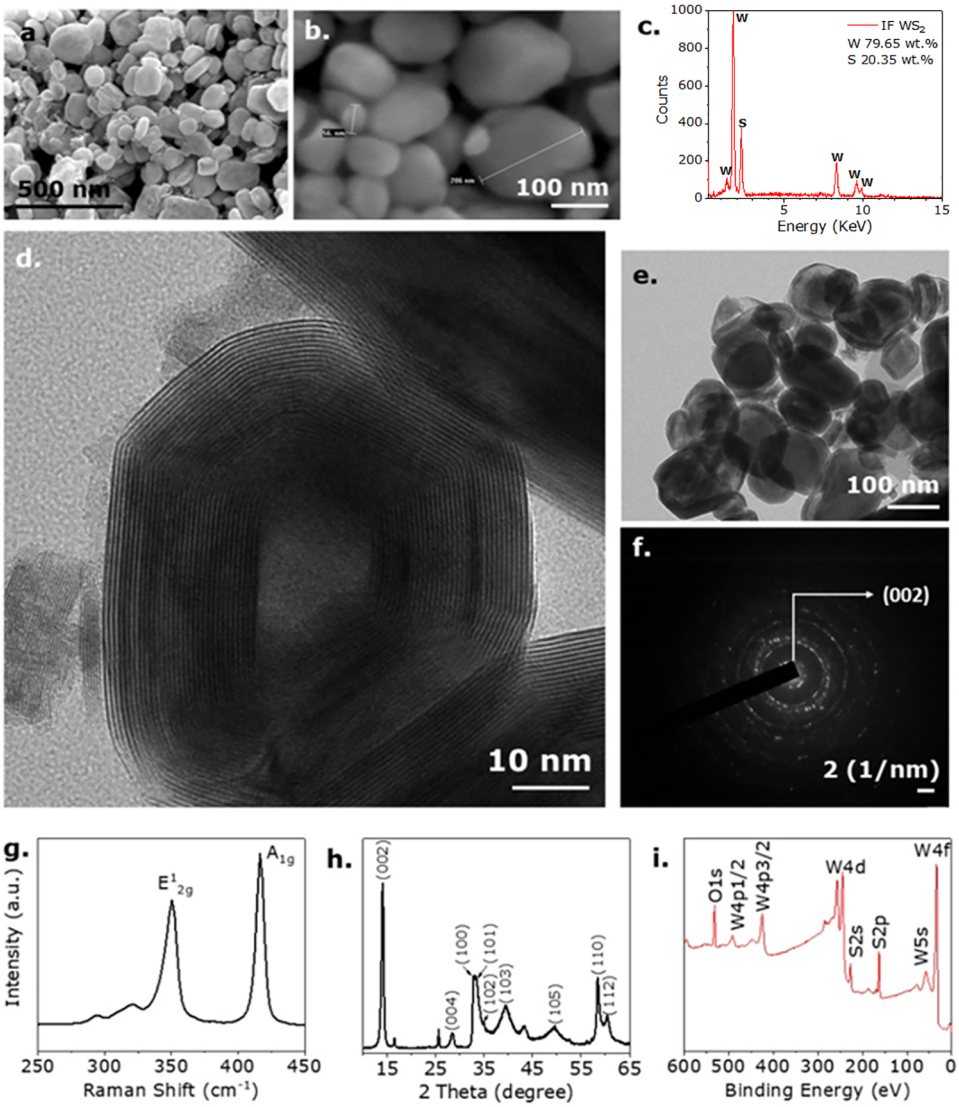

Figure 1. (a) SEM micrograph of the agglomerated WS_2IF nanoparticles. (b) Magnified view of the fullerene-like WS_2 nanoparticles. (c) XRF spectra showing the characteristic elements present in WS_2IF. (d) High-resolution TEM micrograph of the WS_2IF. (e) Demagnified view of the WS_2IF nanoparticle cluster. (f) SAED pattern of the individual WS_2IF particle. (g) Raman spectra of the WS_2IF powder showing the typical position of WS_2 peaks. (h) XRD of of WS2IF nanoparticles. The peaks at 16.5 and 25.6° are likely the result of slight oxidation of particles at the surface defects during specimen preparation or prolonged storage, and (i) XPS survey spectra of WS_2IF nanoparticles.

continuation of a previous study.[22] Similar to typical TMD nanosheets, WS_2IFs suffer from volume expansion and subsequent structural distortion, which lead to inefficient cycling behavior and capacity fading. Therefore, this study utilized upper and lower voltage cutoff techniques to suspend conversion reactions at various stages and observe the structural evolution via differential capacity with evolving cycling conditions. Restriction of voltage cutoff plays a crucial role in maintaining the electrode materials' structural integrity, resulting in consistent and reliable capacity.[23,24] Although energy density and specific capacity decrease with the reduced voltage cutoff (a high upper cut-off), long-term cyclability can be achieved by limiting voltage cutoff for a wide range of applications.[25−27] Grid energy storage devices or portable electronics require numerous cycles over the operational lifetime; hence, ensuring batteries with high cyclability is crucial for sustainable performance.[28−30] Therefore, the kinetics and subtle differences in Na^+- and K^+-ion storage within WS_2IFs were further explored by employing rigorous electrochemical analysis techniques, rendering the preference of charge storage mechanism: faradaic or nonfaradaic. Results showed a higher capacity for Na^+-ion storage and a higher Coulombic efficiency for $Li^+/Na^+/K^+$-ion storage, to preface future studies of efficient storage within quasi-0D fullerene-like nanoparticles.

MATERIALS AND METHODS

Morphological and Spectroscopic Characterization. This study utilized a Hitachi SU8010 scanning electron microscope to collect scanning electron microscopy (SEM) images of the neat WS_2IF material and the spent electrodes. The IXRF system was used to obtain the corresponding X-ray fluorescence (XRF) spectrum, and a Philips CM100 transmission electron microscope was used to obtain the transmission electron microscopy (TEM) images of the bulk WS_2IF material. Raman spectra of the neat material and spent electrodes were obtained by using a Renishaw inVia Raman microscope with a 532 nm laser. X-ray photoelectron

https://doi.org/10.1021/acsomega.3c09758
ACS Omega 2024, 9, 17125−17136

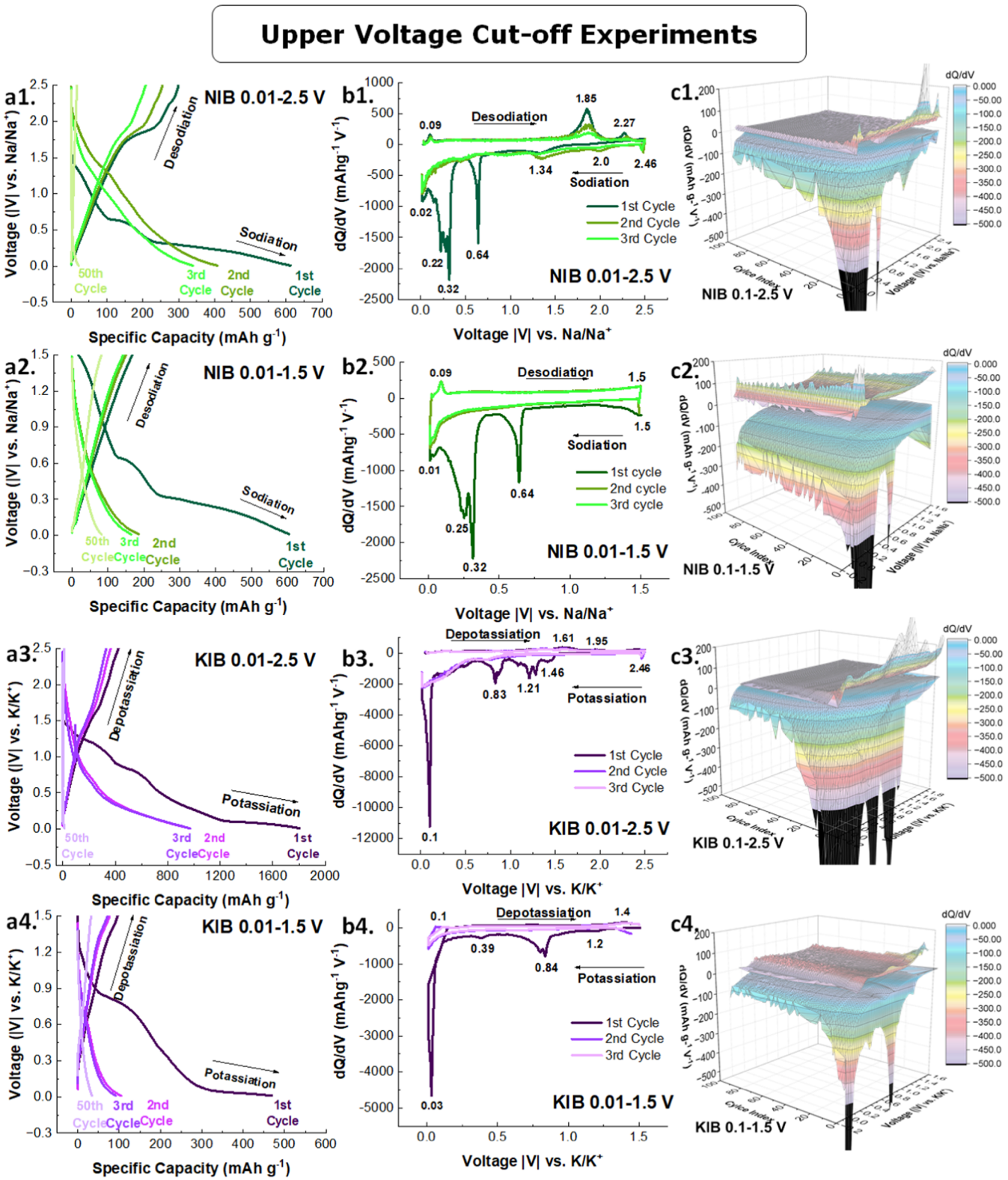

Figure 2. GCD curves of the upper voltage cutoff: (a1) NIB 0.01−2.5 V; (a2) NIB 0.01−1.5 V; (a3) KIB 0.01−2.5 V; and (a4) KIB 0.01−1.5 V half-cells. Differential capacity curves of (b1) NIB 0.01−2.5 V; (b2) NIB 0.01−1.5 V; (b3) KIB 0.01−2.5 V; and (b4) KIB 0.01−1.5 V half-cells. Differential capacity curves plotted as a function of cycle index for (c1) NIB 0.01−2.5 V; (c2) NIB 0.01−1.5 V; (c3) KIB 0.01−2.5 V; and (c4) KIB 0.01−1.5 V half-cells.

spectroscopy (XPS) data were obtained using a Thermo Fisher scientific instrument equipped with a monochromatic Al anode Kα (hν = 1486.6 eV) with in situ sputtering of Ar^+ at 3.0 keV for 120 s. X-ray diffraction (XRD) data were collected via a PANalytical Empyrean instrument with 45 kV, a 40 mA power setting, and a step size of 0.02°.

Preparation of WS_2 IFs. IF nanoparticles of WS_2 were synthesized via the combined sulfurization-reduction solid−gas

https://doi.org/10.1021/acsomega.3c09758
ACS Omega 2024, 9, 17125−17136

reaction[31] of tungsten oxide with H_2S/H_2 gases at elevated temperatures of 750−900 °C. A special design of the quartz-made fluidized-bed reactor was developed for this synthetic process.[2] The size and the shape of the precursor WO_3 semispherical nanoparticles (NPs) preprepared via a separate low-temperature wet-chemistry process were essential for the success of the following growth of WS_2IF. A fast reaction of H_2S and H_2 gases with the oxide NP surface leads to the quick formation of a few closed WS_2 layers encapsulating the oxide core. The oxide core becomes partially reduced to WO_{3-x} and, subsequently, a slow diffusion-controlled reaction leads to full replacement of the oxygen with sulfur atoms. This surface-inward reaction proceeds in a layer-by-layer epitaxial-like fashion, using the external tungsten sulfide layers as a template, until the synthesis of the hollow WS_2IF NPs is completed. Therefore, the size and shape of the fullerene-like NPs are determined by the size and shape of the precursor NPs. The surface passivation of the oxide NPs by the inert layers of WS_2 in the initial stage of the reaction, as well as using a fluidized-bed reactor providing "boiling" of the powder downstream of the gases, prevents coarsening of the NPs during their growth. The majority of precursor tungsten oxide, as well as the IF NPs, ranges from 150 to 350 nm in diameter being of oval or polyhedral shape. The presence of a hollow core in the IF NPs is attributed to the differences in the specific gravity of WS_2 and WO_3 (7.5 and 7.15 g cm^{-3}, respectively) and to the described growth mechanism, where the diameter of the WO_3 NP dictates the diameter of the external layers of each WS_2IF NP.

Electrochemical Measurements. The working electrode for all three cell types was prepared with 70 wt % of the active material (WS_2IF), 15 wt % of carbon black as a conducting agent (Alfa Aesar, MA), and 15 wt % of poly(vinylidene fluoride) (PVDF) as a binder (Alfa Aesar, MA). After preparing a homogeneous slurry by dissolving the materials in 1-methyl-2-pyrrolidinone (Sigma-Aldrich, MO), acting as a solvent for PVDF, a coating (125 μm) on top of a 9 μm thick copper foil was deposited. The slurry coating was dried at 80 °C overnight and punched into 14.29 mm diameter circles as working electrodes. CR-2032-type coin cells were then assembled using the working electrode and Li/Na/K metals as reference and counter electrodes, in the case of LIB/NIB/KIB cells, respectively. Assembly of the half-cells was conducted inside a high-precision ultrapure Ar glovebox with O_2 and H_2O contents below 0.1 ppm. The electrolyte for the LIB (lithium-ion battery)/NIB (sodium-ion battery)/KIB (potassium-ion battery) half-cells consisted of $LiPF_6$/$NaClO_4$/KPF_6 salt in a common solvent: (1:1 v/v) ethylene carbonate (EC)/dimethyl carbonate (DMC) (anhydrous, 99% Sigma-Aldrich). A glass separator soaked with an electrolyte separated the two electrodes in the half-cells. Assembled half-cells were cycled at a constant 100 mA g^{-1} current density for 100 cycles in the Arbin BT 2000 test unit. Cyclic voltammetry (CV) tests were conducted in a CH Instruments electrochemical analyzer (model 600 E) at different scan rates. After cycling the half-cells in specific conditions, cycled electrodes were decrimped in an inert Ar atmosphere and washed with DMC solvent to remove the separator fibers attached to the electrodes for further spectroscopic and microscopic analysis.

RESULTS AND DISCUSSION

The morphology of the WS_2IF nanoparticles was investigated by using SEM and TEM. SEM images (Figure 1a,b) of the WS_2IF showed the pure phase of the quasi-spherical nanoparticles at different magnifications. The XRF spectra (Figure 1c) of the WS_2IF demonstrated the presence of W and S elements. The high-magnification SEM (Figure 1b) and TEM (Figure 1d,e) images of the WS_2IF showed that the shape of the fullerene-like nanoparticle was nearly isotropic and synonymous with the electron micrographs in previously published articles.[2,31] The TEM micrograph (Figure 1d) also shows the polyhedral and quasi-spherical morphology typical for multiwalled WS_2IF.[32] Here, the nanoparticle exhibits an onion-like nested arrangement of several closed layers of WS_2 with a hollow core. According to TEM, the semispherical nanoparticles primarily had closed structures with an average diameter of 100 nm. A selected area electron diffraction (SAED) pattern (Figure 1f) obtained from one of the WS_2IF nanoparticles showed the characteristic 6-fold hexagonal symmetrical spot pattern. This pattern represented the (002) reflection from the WS_2 crystal structure, characteristic of the van der Waals (vdW) plane perpendicular to the electron beam. The SAED ring pattern proves the curved nature of the cage-like WS_2IF particles.[33]

Figure 1g shows the Raman spectrum of the WS_2IF nanoparticles. Two intense peaks in the Raman spectrum of crystalline IF nanoparticles were observed at 349 and 416 cm^{-1}. These peaks were assigned to characteristic E_{2g}^1 and A_{1g} modes of WS_2,[34] corresponding to molecules' in-plane and out-of-plane vibrations, respectively.[14] XRD was utilized to confirm the hexagonal phase of WS_2IF (Figure 1h). The most prominent reflection at 14.08° in the XRD pattern was assigned to the (002) peak, which shifted to lower angles (higher *d*-spacing between the layers) as compared to typically found at 14.32° for neat WS_2 nanosheets, indicating strain in the layered structure of WS_2IF nanoparticles.[31] The broad (004), (101), (103), and (112) peaks, characteristic of the WS_2 phase, reflect the small crystalline size of WS_2IF nanoparticles and the high strain in curved WS_2 layers.[14] Thus, Raman spectroscopy and XRD confirmed the presence of pristine WS_2IF, while the hollow core observed in the TEM image (Figure 1d) indicates the full conversion of the precursor WO_3 nanospheres into WS_2 layered IFs, as followed from the growth mechanism of these nanostructures.[31] However, the XRD pattern of Figure 1h reveals two additional peaks at 16.5 and 25.6°, which were assigned to the slight oxidation of particles at the surface defects during sample preparation or during prolonged storage of the IF nanoparticles under atmospheric conditions, resulting in the appearance of the $WO_3{\cdot}H_2O$ phase (ICDD # 04-01106939). These peaks exhibit a relatively low intensity and represent minor oxidation of the nanoparticles. Fortunately, this issue can be easily resolved by using proper storage and preparation conditions.

Galvanostatic charge−discharge (GCD) curves (Figure 2a1−a4) and derived differential capacity curves (Figure 2b1−b4) offer insights into various reactions that occur at the discharging (sodiation/potassiation) and charging (desodiation/depotassiation) of the NIB and KIB half-cells. Two-dimensional (2D) differential capacity curves in Figure 2b1−b2 demonstrate the multistep first-cycle sodiation process (Figure 2b1) at 0.01−0.32 and 1.34 V. The combination of significant peaks and peaks in the shoulder in the 0.01−0.64 V region may be ascribed to several reactions: insertion of Na^+ ions, conversion reaction of WS_2IF with Na^+ ions into metallic nanoparticles in the Na_2S matrix, and the formation of the

https://doi.org/10.1021/acsomega.3c09758
ACS Omega 2024, 9, 17125−17136

solid−electrolyte interphase (SEI) layer.[35] Most of these reactions are irreversible and predicted due to the disappearance of the peaks in consecutive cycles. Reversible sodiation of WS_2IF nanoparticles was observed as peaks visible in the second and third cycles in the 1.34, 2.0, and 2.46 V regions, thereby indicating the possibility of insertion, conversion, and SEI layer formation. In the desodiation process, significant peaks in the 1.7−1.9, 2.27, and 2.5 V regions may be likely due to the extraction of Na^+ ions from the WS_2IF particles and the reconversion of W into WS_2.[36] In the cell cycled at 0.01−1.5 V (Figure 2b2), the same reactions were observed except at 1.5 V, which could be a partial reaction from the 1.7 V peak.

To assess the continuation and structural distortion of the electrode material, this study also investigated the differential capacity curves as a function of the cycle index, as shown in Figure 2c1−c4. Figure S1a1−b2 are derived surface plots from the 3D differential capacity curves. As demonstrated in the sodiation and desodiation surface plots in Figure S1a1,a2 for NIB 0.01−2.5 V cells, all of the peaks disappeared within the 20th cycle, except for peaks in the low-voltage region. However, NIB cells cycled within the 0.01−1.5 V range showed peaks at 0.09 V and 1.5 V in the sodiation cycle up to a prolonged period (Figure S1b1). Similarly, during desodiation (Figure S1b2), the 0.01 and 0.25 V peaks retained their intensity through 100 cycles, thereby bolstering this study's initial hypothesis: voltage cutoff restricts WS_2IF structure pulverization, even for repeated large Na^+-ion insertion/extraction.

Similar to the sodiation/desodiation process, the potassiation/depotassiation process of the WS_2IF electrodes is demonstrated in the GCD plots in Figure 2a3,a4. Differential capacity curves derived from the GCD graphs elucidate the specific reaction at particular voltages. In the first potassiation process (Figure 2b3), major peaks are observed in the 0.1, 0.83, 1.0, 1.5, and 2.46 V regions. Previous investigations have assigned the peaks above the 0.75 V region to the intercalation process and the peaks below the 0.75 V region to a mixture of reactions from the interaction of K^+ ions with the WS_2 material, conversion reactions, and the formation of SEI layers.[37−39] Other studies have designated the interaction of K^+ ions with WS_2-based materials to be purely intercalation-based since no trace of metallic W was found due to conversion reaction products.[27,40] Although this study refrained from assigning peaks to certain reactions due to lack of direct evidence, the peak at 0.1 V for the 0.01−2.5 V cell displayed the highest intensity, indicating increased electron transfer due to the SEI layer formation reaction in general. Previous research where MoS_2 was utilized as the anode material with KPF_6 as an electrolyte salt resulted in unstable, potassium fluoride-deficient, organic species-rich SEI layer formation that led to poor capacity retention.[41]

The continuation of the peaks in 3D differential capacity curves is presented in Figure 2c3,c4. Further elucidation of the 3D differential capacity curves is provided in Figure S2a1−b2 of potassiation/depotassiation processes for two cells cycled at separate voltage ranges. Figure S2a1,a2 of the potassiation/depotassiation processes for the cells cycled in the 0.01−2.5 V range reveals no continuation of reactions from high voltage ranges; peaks in the 1.0−1.5 V region discontinued after the 10th cycle. The only reactions that continued were in the lower voltage region (0.01 V peak in the potassiation cycle, which faded gradually after the 50th cycle, shown in Figure S2a1). However, when the upper voltage cutoff technique was utilized for the KIB 0.01−1.5 V cell, the combined peaks in the 0.01−0.3 V region maintained a similar intensity during the prolonged process (Figure S2b1). In the depotassiation step, continuity of the 1.4 V peak was evident due to a partial reaction from the 1.7 V peak up to the 100th cycle. Furthermore, the peak at 0.1−0.8 V maintained its intensity throughout the 100th cycle of the depotassiation process (Figure S2b2), indirectly indicating structural preservation of the WS_2IF particles in KIB 0.01−1.5 V cells.

To compare Na^+- and K^+-ion storage with Li^+-ion storage, two LIB cells were assembled and tested at the same conditions (0.01−1.5 V and 0.01−2.5 V). Corresponding to GCD, derived differential capacity curves are presented in Figure S3a1−c2. For the 0.01−2.5 V LIB cell, the first lithiation cycle includes sharp peaks at 1.7, 0.79, 0.67, and 0.01 V (Figure S3b1). The responses at lower voltage ranges may be ascribed to a combination of reactions: insertion of Li^+ ions into WS_2IF layers, additional conversion reaction of WS_2 and Li^+ ions to form W and Li_2S matrices, irreversible electrolyte decomposition, and the formation of solid electrolyte interface layers.[42−44] Except for the 0.01 V peak, the other peaks did not appear in the second and third cycles, indicating the irreversibility of the reactions. However, the delithiation curves present a significant peak at 2.3 V and a shoulder peak at 2.0 V that possibly originate from the extraction of Li^+ ions from the Li_xWS_2 host. Additional reversible peaks in the second and third lithiation cycles may be attributed to the further insertion of Li^+ ions into the interlayers of WS_2IF.[45] For the LIB cells cycled at the 0.01−1.5 V range (Figure S3b2), the same reactions indicated by the same peaks are present as expected.

To further examine the reaction continuity or polarization of the peaks, individual lithiation/delithiation visible in 3D differential curves (Figure S3c1,c2) is demonstrated as surface plots in Figure S4a1−b2. During the lithiation process, the peaks at 0.75 and 1.25 V diminish in the very early stages (20th cycle and 40th cycle, respectively). Although the peaks around 1.75−2.25 V continue further, they nevertheless fade out in the 80th cycle for the 0.01−2.5 V cell (Figure S4a1). The only peak consistent with its intensity is the 1.5 V peak for the 0.01−1.5 V cell. As shown for the LIB 0.01−2.5 V cells (Figure S4a2), during delithiation, specific reactions at approximately 1.8 V continued only to 20−25 cycles. The only long-term reaction during continuous cycling appeared at 2.3 V and then gradually lost intensity, indicating a decrease in the number of electron transfers and fading after the 80th cycle. In the delithiation process (Figure S4a2), specific peaks at 1.7, 0.79, and 0.67 V diminished during the 40th cycle, indicating the discontinuation of the reactions. Shoulder peaks around 1.5 V started to fade in the 15th cycle and ceased in the 40th cycle. As shown, major 2.0 V peaks also gradually faded beginning in the 20th cycle and disappeared entirely after the 80th cycle. Slight hysteresis was also demonstrated from the 2.0 V peak. Only the low-voltage region of the 0.01 V peak continued through the 100th cycle. The discontinuation of peaks may nonetheless be ascribed to mechanical stress generation within the WS_2IFs and structure pulverization upon repeated Li^+-ion insertion/extraction.[46−48] A possible explanation for reaction peak discontinuation might be that the structure completely changes after specific cycles due to repeated cycling; therefore, no reaction proceeds further because no sites are available. Comparatively, for the 0.01−1.5 V cell, during lithiation, cumulative peaks around 0.01−0.6 V maintain their intensity in Figure S4b1. Specific peaks at 0.01 V during delithiation

https://doi.org/10.1021/acsomega.3c09758
ACS Omega 2024, 9, 17125−17136

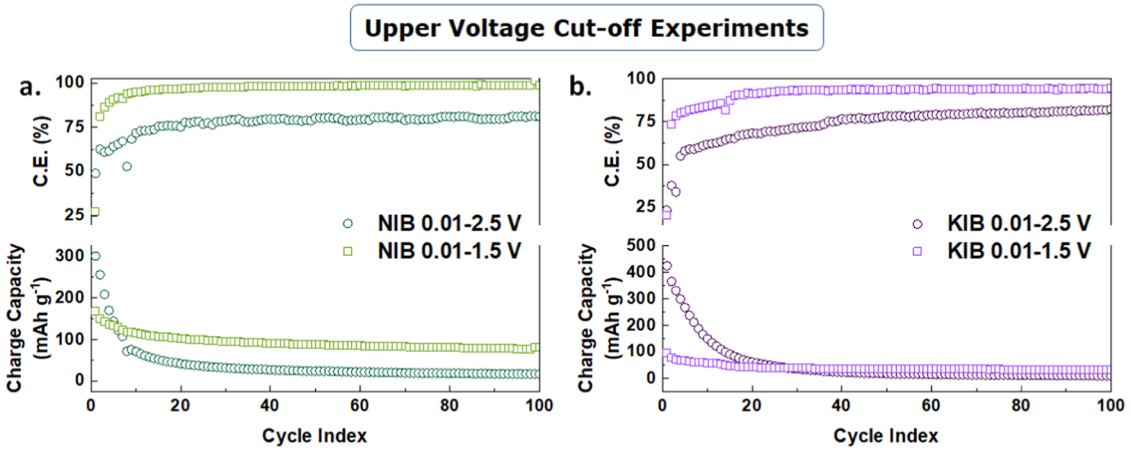

Figure 3. Cycling stability and Coulombic efficiency of (a) NIB 0.01−2.5 V and NIB 0.01−1.5 V half-cells; and (b) KIB 0.01−2.5 V and KIB 0.01−1.5 V half-cells.

were more prominent (Figure S4b2), and no peak plummeting behavior was evident. A partial reaction/partial peak (possibly arising from outside the 1.5 V window) limited to 1.5 V due to voltage cutoff continues up to the 100th cycle, thereby indicating the efficiency of a high upper voltage cutoff technique.

Cycling performances derived from GCD experiments for NIB and KIB systems were measured at a constant current density of 100 mA g^{-1}. The specific capacity achieved from cells at different potential ranges was plotted as a function of the cycle index (Figure 3a,b), from which the Coulombic efficiency of the electrode material was also calculated. The 0.01−2.5 V NIB cell displayed a first-cycle charge capacity of 299 mAh g^{-1} with a Coulombic efficiency of 48.94%, which greatly exceeded the 0.01−1.5 V cell at 167.65 mAh g^{-1} with a Coulombic efficiency of 27.69%. However, the NIB 0.01−2.5 V cell never reached a Coulombic efficiency near 100%, whereas the 0.01−1.5 V cell reached a Coulombic efficiency near 100% after 10 cycles. As a result, capacity retention of the NIB cell with no voltage cutoff technique was much lower (i.e., sudden capacity degradation was observed up to the eighth cycle), which was quickly overtaken by the NIB 0.01−1.5 V cell in the fifth cycle. These behaviors of the NIB 0.01−2.5 V cells corresponded to findings from the 3D differential capacity curves (Figure 2c1,c2) and surface plots (Figure S1a1−b2), where maintenance of specific peaks for the 0.01−1.5 V cell was perceived. Notably, this is the opposite characteristic of the 0.01−2.5 V cell. This phenomenon strongly suggests that Na^+-ion insertion/extraction at high voltage ranges may lead to permanent structure distortion for which lesser capacity is achieved at prolonged cycling processes, even for WS_2IF nanoparticles that differ from nanosheets. For example, in the 100th cycle, the specific capacity of the 0.01−2.5 V cell was 16.97 mAh g^{-1}, compared to 81.63 mAh g^{-1} for the 0.01−1.5 V NIB cell.

Similar characteristics were observed for the two KIB cells from Figure 3b, where the first-cycle specific charge capacity for the 0.01−2.5 V cell was 423 mAh g^{-1} with a Coulombic efficiency of 23.47%. A similar Coulombic efficiency was perceived for the 0.01−1.5 V KIB cell, as highlighted in the previous section (KPF_6 electrolyte degradation). Similar to the NIB cells, the Coulombic efficiency of the KIB cells with a high upper voltage cutoff dominated the cell cycled up to 2.5 V, reaching nearly 100% but at a later stage (after the 20th cycle). This performance could be connected to the results obtained from the surface plots (Figure S2a1−b2). Although it has a higher capacity retention, the 0.01−2.5 V cell demonstrated a higher specific capacity in the 100th cycle (32 mAh g^{-1}, compared to 9.43 mAh g^{-1} of the 0.01−2.5 V cell). However, the specific charge capacity of the KIB ce.lls was far lower than the NIB cells, providing overall inefficiency of large K^+-ion storage within closed cage-like structures of WS_2IF.

Figure S5 depicts the cycling of two LIB cells at different voltage ranges under the same conditions as those for the NIB and KIB cells. The LIB cell cycled within 0.01−2.5 V demonstrated a specific charge capacity of 349.67 mAh g^{-1} in the first cycle with a Coulombic efficiency of 42%. Consistent capacity degradation behavior was observed starting from the second cycle and perpetuating throughout the long-term cycling process. Capacity fading of the 0.01−2.5 V cell could be well correlated with observations from the 3D differential capacity plots, where cessation of specific reactions occurred, suggesting that structural distortion might be taking place. First-cycle capacity loss was ascribed to inevitable SEI layer formation and a combination of side reactions through which Li^+ ions were irreversibly consumed.[49] Notably, the Coulombic efficiency of the 0.01−2.5 V LIB cell was always 60−70%, although the LIB cell cycled at a high upper cutoff voltage displayed 233.62 mAh g^{-1} initial capacity with a Coulombic efficiency of 30.52%. The lower Coulombic efficiency was correlated with the increased intensity of the peak attributed to SEI layer formation (Figure S4a1), where increased Li^+-ion consumption was predicted, resulting in a very high first-cycle specific discharge capacity of 824.69 mAh g^{-1} (Figure S3a1). Nevertheless, the Coulombic efficiency of the 0.01−1.5 V LIB cell was consistently near 100% from the sixth cycle, resulting in improved capacity retention with no fading. The better capacity retention was also correlated with the prolongation of the reaction peaks from the surface plots shown in Figure S4b1,b2. The GCD and differential capacity curve shown in Figure S6 along with the cycling stability curve in Figure S7 exhibited the effect of a lower voltage cutoff compared to the upper voltage cutoff experiment.

The fast physical charge storage mechanism within the WS_2IF material was studied using CV experiments at various scan rates.[50] The charge storage process typically relies on different scan rates (ν, mV s^{-1}) in CV experiments, where the current response (i, amp) fluctuates as a function of voltage

https://doi.org/10.1021/acsomega.3c09758
ACS Omega 2024, 9, 17125−17136

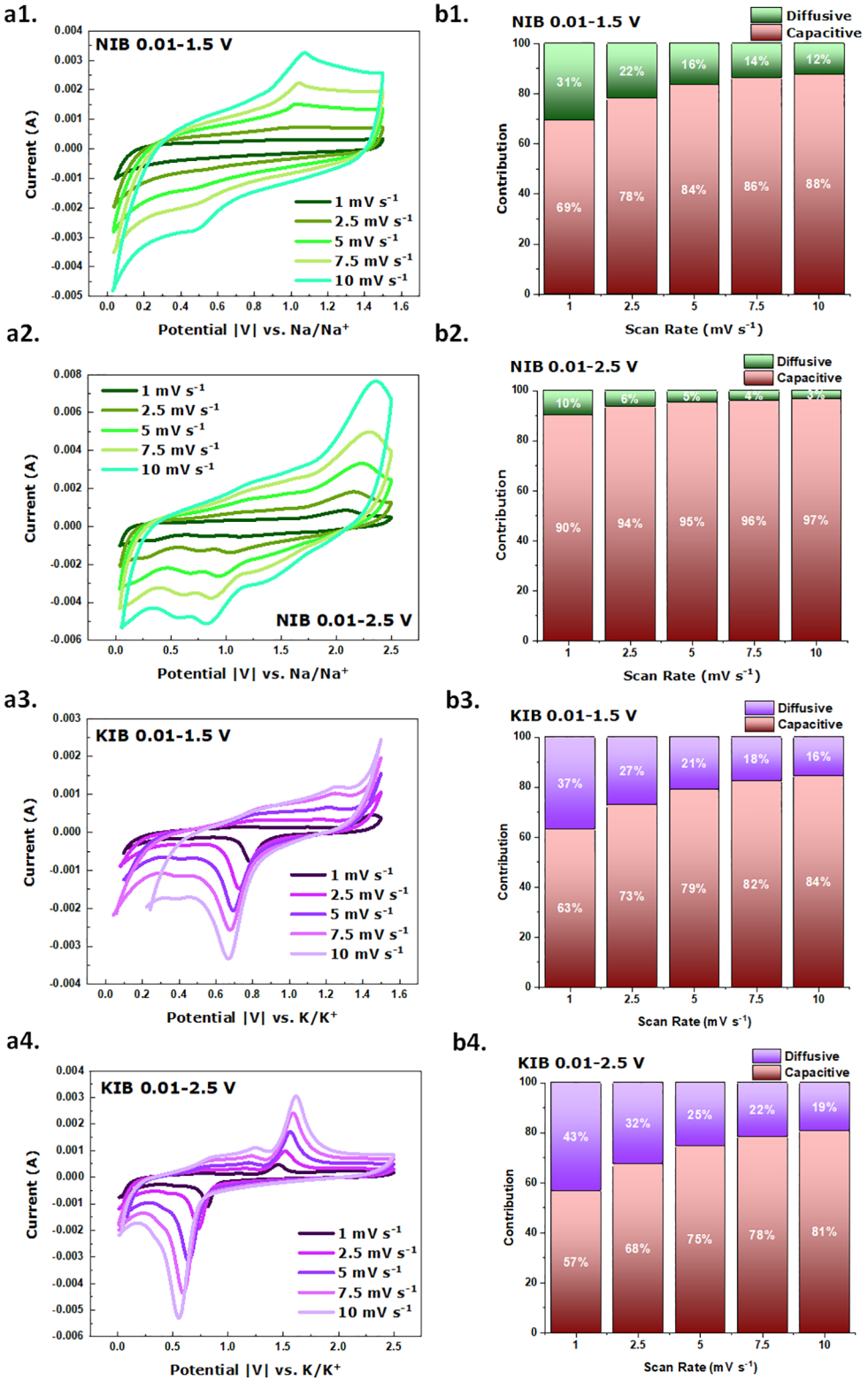

Figure 4. CV curves of (a1) NIB 0.01−1.5 V, (a2) NIB 0.01−2.5 V, (a3) KIB 0.01−1.5 V, and (a4) KIB 0.01−2.5 V half-cells. Capacitive and diffusion-controlled contribution ratios for different scan rates of (b1) NIB 0.01−1.5 V, (b2) NIB 0.01−2.5 V, (b3) KIB 0.01−1.5 V, and (b4) KIB 0.01−2.5 V half-cells.

sweeps. Figure 4a1−a4 shows the CV curves for the NIB and KIB cells cycled at different voltage ranges, respectively, while Figure S8a1,a2 illustrates the CV curves from the LIB cells cycled at two different voltage ranges. Five different scan rates, 1, 2.5, 5, 7.5, and 10 mV s^{-1}, were utilized to investigate the charge storage mechanism. In Figure 4a1,a2, the reduction peak at 0.53 V can be attributed to the conversion reaction with residuals of the oxide precursor ($WO_3 + 6Na^+ + 6e^- \leftrightarrow 3Na_2O + W$).[51,52] Similarly, for KIBs in Figure 4a3,a4, reduction peaks at 0.46 V can be ascribed to the reduction

https://doi.org/10.1021/acsomega.3c09758
ACS Omega 2024, 9, 17125−17136

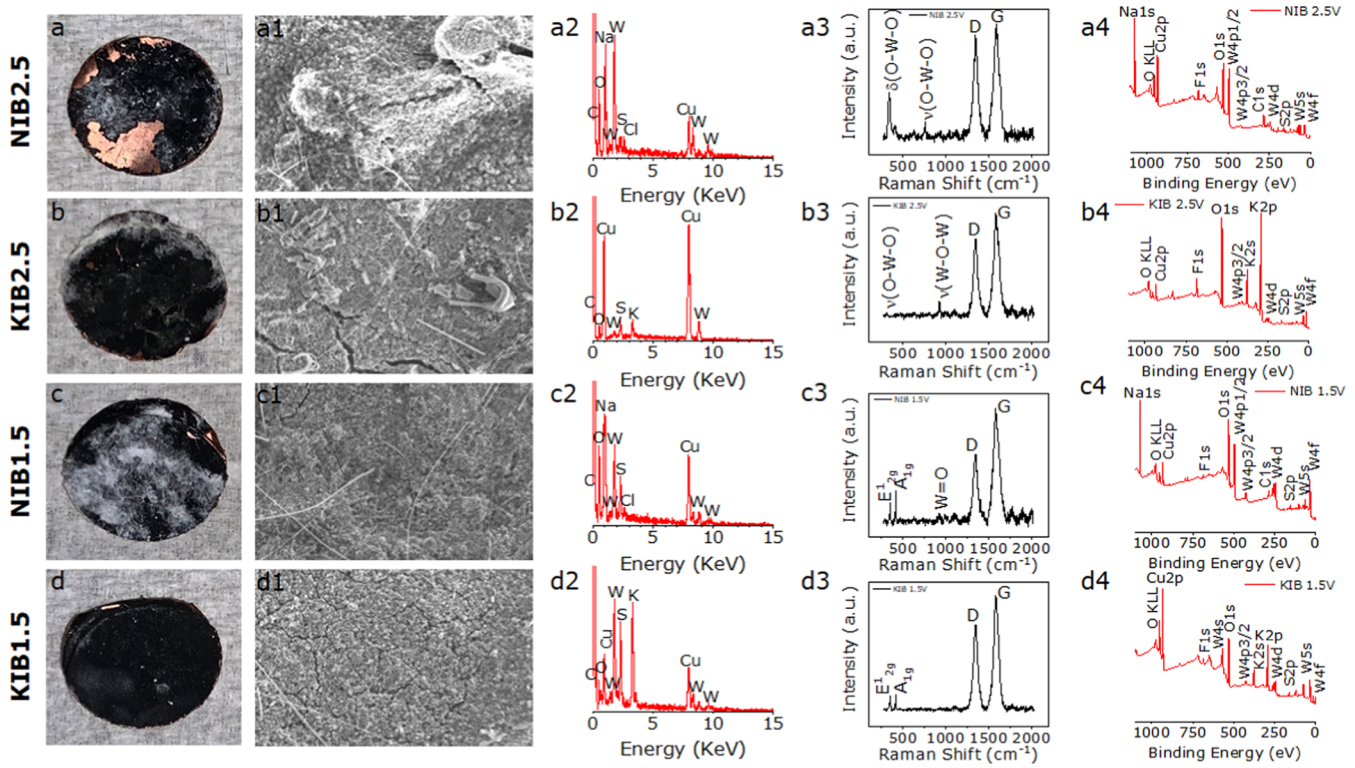

Figure 5. Structural characterization of the spent (cycled) NIB and KIB electrodes. (a−d) Digital camera image. (a1−d1) SEM micrographs showing structural integrity of the spent electrodes after cycling. (a2−d2) XRF spectra of the electrodes identifying the characteristic elements. (a3−d3) Raman spectra showing the distinctive peaks obtained for the spent electrodes. (a4−d4) XPS survey scan of the electrodes representing the presence of individual elements after cycling.

peak of WO_{3-x}.[53] In the framework of this analysis, examination of the CV profiles enabled quantitative differentiation of two charge storage mechanisms: nonfaradaic surface capacitive effects and faradaic diffusion-controlled insertion processes,[54] according to eq 1.

$$i(V) = k_1\nu + k_2\nu^{1/2} \quad (1)$$

The rearrangement of eq 1 established a relationship in $i(V)/\nu^{1/2}$ vs $\nu^{1/2}$ plots because k_1 (slope) and k_2 (y-axis intercept) follow a linear behavior, as shown in Figure S9a1−b3, for six cell types cycled at different voltage ranges at fixed potentials, neglecting minimal peak shifts. Notably, $k_1\nu$ and $k_2\nu^{1/2}$ in the equation denote the surface capacitive and intercalation-based diffusive charge storage process, respectively, as illustrated in Figure 4b1−b4 for NIB and KIB cells cycled at two different potential ranges as a function of employed scan rates. The 31, 22, 16, 14, and 12% contributions for the NIB 0.01−1.5 V cells (Figure 4b1) and the 10, 6, 5, 4, and 3% contributions for the NIB 0.01−2.5 V cells (Figure 4b2) were from diffusive processes at scan rates of 1, 2.5, 4, 7.5, and 10 mV s^{-1}, respectively. Finally, the 37, 27, 21, 18, and 16% contributions for the KIB 0.01−1.5 V cells (Figure 4b3), and the 43, 32, 25, 22, and 19% contributions for the KIB 0.01−2.5 V cells (Figure 4b4) were from diffusive processes at scan rates of 1, 2.5, 4, 7.5, and 10 mV s^{-1}, respectively. Although the LIB cells cycled at 0.01−1.5 V displayed 49, 38, 30, 26, and 23% pseudocapacitive contributions (Figure S8b1,b2), the cell cycled at 0.01−2.5 V demonstrated 69, 58, 49, 44, and 41% for scan rates of 1, 2.5, 4, 7.5, and 10 mV s^{-1}, respectively.

To summarize, an increase in the capacitive contribution as a function of gradually increasing scan rate was common to all six cells, as previously observed for electrodes with fast reaction kinetics. As the scan rate increases, alkali-metal ions generally experience decreased periods of complete diffusion inside the electrode material. Therefore, the cations prefer a surface-adsorption-based storage mechanism rather than the formation of a solid solution. Dominance in the capacitive contribution was observed from the NIB, KIB, and LIB cells cycled at high upper cutoff voltages.[55−57] As shown in the charge−discharge curves, high cutoff voltages yielded less capacity than the other cells, meaning the alkali-metal ions had less time to interact with the host WS_2IF electrode. Study results revealed that some of the reactions (intercalation and conversion) for the LIB and NIB cells exceeded the 0.01−1.5 V range, as 2D and 3D differential capacity curves, proving that high cutoff voltages may suppress specific reactions. Finally, the cage-like WS_2IF semispherical nanoparticles may also significantly impact the charge storage mechanism, as shown in a previous study.[14] Future research efforts must corroborate this conclusion, which is currently underway. The height of the anodic peak (1.5 V) in the negative current axis for the 0.01−1.5 V KIB cell was pronounced, indicating more electrons are transferred due to partial reactions than the complete reaction of the 0.01−2.5 V cell, thereby indirectly affirming the initial hypothesis of this study that a high voltage cutoff extends protection of the WS_2IF structure. This technique could be explored with a combination of composite structure formation to realize the full potential of voltage cutoff experiments since some composite structure formation techniques have been

https://doi.org/10.1021/acsomega.3c09758
ACS Omega 2024, 9, 17125−17136

shown to enhance the capacity and stabilize the electrochemistry of TMD-based nanomaterials.[58,59]

The upper voltage cutoff (2.5 and 1.5 V) electrodes were disassembled after cycling and analyzed using characterization techniques shown in Figure 5. Digital camera images of the recovered spent electrodes after cycling are shown in Figure 5a−d. The spent electrodes, particularly the NIB 0.01−2.5 V electrode, showed partial disintegration during the disassembly process. The white substance on the electrodes was the residual waste of the glass fiber separators used to assemble the cells. However, the spent electrodes showed no visible color change or imperfections. The presence of glass fibers from the separator was confirmed by SEM images (Figure 5a1−d1) of the spent electrodes. SEM images of the 0.01−2.5 V electrodes showed more microcracks compared to the 0.01−1.5 V electrodes, revealing the structural integrity and minimal stress development within the 0.01−1.5 V electrodes during cycling. Figures 5a2−d2 and S10 present a qualitative elemental analysis of the spent electrodes and neat electrodes characterized by the XRF technique, respectively. Characteristic peaks for W and S spectral lines were observed for all of the electrodes, suggesting the existence of individual elements like W and S after cycling. In addition, characteristic peaks for the electrolyte used in different cells (i.e., Na and Cl for NIBs, K and F for KIBs) were identified by the XRF. Cu peaks, originating from the Cu foils, were also detected. The elemental compositions obtained from the XRF spectra of spent NIB and KIB electrodes are summarized in Tables ST1 and ST2, respectively.

This study also utilized Raman spectroscopy to determine the spent electrode microstructure and to designate the WS_2 phase from the carbon structure. Figure 5a3−d3 shows the Raman spectra of the electrodes after cycling. Two intense peaks at ∼1350 and ∼1599 cm^{-1} were assigned to the D and G carbon vibrations bands, respectively.[60] For the 0.01−2.5 V spent electrodes (Figure 5a3,b3), additional Raman spectrum for crystalline WO_3 was observed. Intense peaks at 924, 808, and 305 cm^{-1} corresponded to the stretching vibrations of the bridging oxygen and were associated with W−O, W−O−W stretching (ν), and O−W−O bending (δ) vibrational modes, respectively.[61] In contrast, the 0.01−1.5 V spent electrodes (Figure 5c3,d3) showed Raman peaks at 349 and 416 cm^{-1}, which correspond to the in-plane mode E_{2g}^1 and the out-of-plane mode A_{1g} for WS_2IF, respectively.[34] These results also suggest that WS_2IF electrodes were oxidized at a higher voltage window (0.01−2.5 V), contributing to degradation of the cells. The Raman spectra of the 0.01−1.5 V NIB cells are similar to the spectrum of the neat electrode before cycling (Figure S11). Figure 5a4−d4, which shows the XPS survey scan of the spent electrodes, highlights the presence of C, O, Cl, F, and Cu elements, as well as the base materials of W and S, indicating SEI layer formation. Similar characteristics were also apparent from the postcycling analysis of the LIB cells, presented in Figure S12a−b4.

CONCLUSIONS

This research is the first work to study beyond Li^+-ion storage behavior of a nanocage-like WS_2IF structure. Morphological and chemical characteristics of WS_2 nanoparticles were studied via SEM, TEM, XRF, Raman spectroscopy, XPS, and XRD. This study also sought to determine whether the reduced alkali-metal-ion storage of traditional TMD-based materials is similar for 0D WS_2IF structures. Results showed that side reactions and significant volume changes led to structural distortion. This study also explored the upper and lower voltage cutoff techniques to limit certain reactions. Upper voltage cutoff led to stable capacity with minimal capacity fading and higher Coulombic efficiency gain at prolonged cycling conditions for Li^+-/Na^+-ion storage. Although K^+-ion storage in the upper voltage cutoff range resulted in a higher Coulombic efficiency, no significant benefit of higher capacity gain was apparent. Therefore, this study utilized 3D differential capacity curves and derived surface plots, where reactions for 0.01−2.5 V cells ceased after the 20th cycle, indicating structural pulverization that resulted in capacity fading, also detectable from postcycling analysis. In addition, a lower voltage cutoff with an optimal upper voltage range yielded significantly reduced capacity gain because some reactions were restricted, resulting in less electron transfer. The CV experiments revealed that all three systems (LIB/NIB/KIB) with a high upper voltage cutoff displayed preference in the nonfaradaic charge storage mechanism, regardless of ion size. This study lays the groundwork for the use of TMD-based composites combined with a suitable voltage cutoff during cell cycling for next-generation electrochemical energy storage devices.

ASSOCIATED CONTENT

Supporting Information

The Supporting Information is available free of charge at https://pubs.acs.org/doi/10.1021/acsomega.3c09758.

Data for surface plots derived from 3D differential capacity curves for NIB half-cells (Figure S1), KIB half-cells (Figure S2), GCD and differential capacity curves of LIB half-cells (Figure S3), surface plots of LIB half-cells (Figure S4), cycling stability test of LIB half-cells (Figure S5), GCD and differential capacity curves of NIB and KIB half-cells (Figure S6) for lower voltage cutoff experiments, cycling stability tests of NIB and KIB half-cells with a lower voltage cutoff (Figure S7), CV curves and capacity contribution bar charts for LIB half-cells (Figure S8), linear fitting of voltammetric sweeps for three different half-cells (Figure S9), XRF spectrum (Figure S10) and Raman spectrum (Figure S11) of neat electrodes, tabulated elemental wt % composition of spent NIB (Table ST1) and KIB (Table ST2) half-cells, and postcycling analysis figures of spent LIB electrodes (Figure S12) (PDF)

AUTHOR INFORMATION

Corresponding Authors

Sonjoy Dey − *Department of Mechanical and Nuclear Engineering, Kansas State University, Manhattan, Kansas 66506, United States;* orcid.org/0000-0001-6244-2750; Email: sonjoy@ksu.edu

Gurpreet Singh − *Department of Mechanical and Nuclear Engineering, Kansas State University, Manhattan, Kansas 66506, United States;* orcid.org/0000-0003-2126-9204; Email: gurpreet@ksu.edu

Authors

Arijit Roy − *Department of Mechanical and Nuclear Engineering, Kansas State University, Manhattan, Kansas 66506, United States;* orcid.org/0009-0004-8026-2330

https://doi.org/10.1021/acsomega.3c09758
ACS Omega 2024, 9, 17125−17136

Shakir Bin Mujib − *Department of Mechanical and Nuclear Engineering, Kansas State University, Manhattan, Kansas 66506, United States;* orcid.org/0000-0002-6699-420X

Manjunath Krishnappa − *Department of Physics, Faculty of Sciences, Holon Institute of Technology, Holon 5810201, Israel; Advanced Research Centre for Clean and Green Energy, Department of Chemistry, Nitte Meenakshi Institute of Technology, Bangalore 560064, India*

Alla Zak − *Department of Physics, Faculty of Sciences, Holon Institute of Technology, Holon 5810201, Israel;* orcid.org/0000-0002-3807-3454

Complete contact information is available at: https://pubs.acs.org/10.1021/acsomega.3c09758

Author Contributions

Conceptualization: G.S.; methodology: G.S. and S.D.; WS_2IF synthesis, SEM, and TEM analysis: A.Z. and M.K.; XPS, XRF, and Raman: S.B.M.; cell assembly and data acquisition: S.D.; GCD, CV, differential capacity: A.R.; postcycling analysis: S.B.M.; resources: G.S.; data curation: S.D.; writing—original draft preparation: S.D.; writing—review and editing: G.S. and A.Z; visualization: S.D.; supervision: G.S.; and funding acquisition: G.S. All authors have read and agreed to the published version of the manuscript.

Notes

The authors declare no competing financial interest.

■ ACKNOWLEDGMENTS

This work was supported by the National Science Foundation grants #1743701, 1454151, and 2025298. The research was performed in part in the Nebraska Nanoscale Facility: National Nanotechnology Coordinated Infrastructure and the Nebraska Center for Materials and Nanoscience (and/or NERCF), which are supported by the National Science Foundation under Award ECCS: 2025298, and the Nebraska Research Initiative. The authors would also like to acknowledge useful discussion regarding the preparation of the manuscript from Dr. Reshef Tenne. The authors are thankful to Dr. Yishay Feldman, the Weizmann Institute of Science, for the assistance with XRD measurements, the fruitful discussion and interpretation of XRD results.

■ REFERENCES

(1) Tenne, R. Inorganic nanotubes and fullerene-like nanoparticles. *J. Mater. Res.* **2006**, *21* (11), 2726−2743.

(2) Feldman, Y.; Zak, A.; Popovitz-Biro, R.; Tenne, R. New reactor for production of tungsten disulfide hollow onion-like (inorganic fullerene-like) nanoparticles. *Solid State Sci.* **2000**, *2* (6), 663−672.

(3) Kopnov, F.; Yoffe, A.; Leitus, G.; Tenne, R. Transport properties of fullerene-like WS2 nanoparticles. *Phys. Status Solidi B* **2006**, *243* (6), 1229−1240.

(4) Rapoport, L.; Leshchinsky, V.; Lvovsky, M.; Nepomnyashchy, O.; Volovik, Y.; Tenne, R. Friction and wear of powdered composites impregnated with WS2 inorganic fullerene-like nanoparticles. *Wear* **2002**, *252* (5−6), 518−527.

(5) Adini, A. R.; Redlich, M.; Tenne, R. Medical applications of inorganic fullerene-like nanoparticles. *J. Mater. Chem.* **2011**, *21* (39), 15121−15131.

(6) Liu, Y.-F.; Han, K.; Peng, D.-N.; Kong, L.-Y.; Su, Y.; Li, H.-W.; Hu, H.-Y.; Li, J.-Y.; Wang, H.-R.; Fu, Z.-Q.; Ma, Q.; Zhu, Y.-F.; Tang, R.-R.; Chou, S.-L.; Xiao, Y.; Wu, X.-W. Layered oxide cathodes for sodium-ion batteries: From air stability, interface chemistry to phase transition. *InfoMat* **2023**, *5* (6), No. e12422.

(7) Zhao, C.; Ding, F.; Lu, Y.; Chen, L.; Hu, Y.-S. High-Entropy Layered Oxide Cathodes for Sodium-Ion Batteries. *Angew. Chem., Int. Ed.* **2020**, *59* (1), 264−269.

(8) Xiao, Y.; Liu, Y.-F.; Li, H.-W.; Li, J.-Y.; Wang, J.-Q.; Hu, H.-Y.; Su, Y.; Jian, Z.-C.; Yao, H.-R.; Chen, S.-Q.; Zeng, X.-X.; Wu, X.-W.; Wang, J.-Z.; Zhu, Y.-F.; Dou, S.-X.; Chou, S.-L. Insights into layered−tunnel dynamic structural evolution based on local coordination chemistry regulation for high-energy-density and long-cycle-life sodium-ion oxide cathodes. *InfoMat* **2023**, *5* (10), No. e12475.

(9) Zhao, L.-F.; Hu, Z.; Lai, W.-H.; Tao, Y.; Peng, J.; Miao, Z.-C.; Wang, Y.-X.; Chou, S.-L.; Liu, H.-K.; Dou, S.-X. Hard Carbon Anodes: Fundamental Understanding and Commercial Perspectives for Na-Ion Batteries beyond Li-Ion and K-Ion Counterparts. *Adv. Energy Mater.* **2021**, *11* (1), No. 2002704.

(10) Lei, H.; Li, J.; Zhang, X.; Ma, L.; Ji, Z.; Wang, Z.; Pan, L.; Tan, S.; Mai, W. A review of hard carbon anode: Rational design and advanced characterization in potassium ion batteries. *InfoMat* **2022**, *4* (2), No. e12272.

(11) Jain, R.; Lakhnot, A. S.; Bhimani, K.; Sharma, S.; Mahajani, V.; Panchal, R. A.; Kamble, M.; Han, F.; Wang, C.; Koratkar, N. Nanostructuring versus microstructuring in battery electrodes. *Nat. Rev. Mater.* **2022**, *7* (9), 736−746.

(12) Lei, T.; Chen, W.; Huang, J.; Yan, C.; Sun, H.; Wang, C.; Zhang, W.; Li, Y.; Xiong, J. Multi-Functional Layered WS2 Nanosheets for Enhancing the Performance of Lithium−Sulfur Batteries. *Adv. Energy Mater.* **2017**, *7* (4), No. 1601843.

(13) Song, Y.; Liao, J.; Chen, C.; Yang, J.; Chen, J.; Gong, F.; Wang, S.; Xu, Z.; Wu, M. Controllable morphologies and electrochemical performances of self-assembled nano-honeycomb WS2 anodes modified by graphene doping for lithium and sodium ion batteries. *Carbon* **2019**, *142*, 697−706.

(14) Dey, S.; Manjunath, K.; Zak, A.; Singh, G. WS2 Nanotube-Embedded SiOC Fibermat Electrodes for Sodium-Ion Batteries. *ACS Omega* **2023**, *8* (11), 10126−10138.

(15) Kim, I.; Park, S.-W.; Kim, D.-W. Onion-like crystalline WS2 nanoparticles anchored on graphene sheets as high-performance anode materials for lithium-ion batteries. *Chem. Eng. J.* **2019**, *375*, No. 122033.

(16) Zhang, Y.; Zhang, L.; Lv, Ta.; Chu, P. K.; Huo, K. Two-dimensional transition metal chalcogenides for alkali metal ions storage. *ChemSusChem* **2020**, *13* (6), 1114−1154.

(17) Cai, R.; Bao, L.; Zhang, W.; Xia, W.; Sun, C.; Dong, W.; Chang, X.; Hua, Z.; Shao, R.; Fukuda, T.; Sun, Z.; Liu, H.; Zhang, Q.; Xu, F.; Dong, L. In situ atomic-scale observation of size-dependent (de)potassiation and reversible phase transformation in tetragonal FeSe anodes. *InfoMat* **2023**, *5* (1), No. e12364.

(18) Woo, S. H.; Yadgarov, L.; Rosentsveig, R.; Park, Y.; Song, D.; Tenne, R.; Hong, S. Y. Fullerene-like Re-Doped MoS2 Nanoparticles as an Intercalation Host with Fast Kinetics for Sodium Ion Batteries. *Isr. J. Chem.* **2015**, *55* (5), 599−603.

(19) Wei, S.; Serra, M.; Mourdikoudis, S.; Zhou, H.; Wu, B.; Děkanovský, L.; Šturala, J.; Luxa, J.; Tenne, R.; Zak, A.; Sofer, Z. Improved Electrochemical Performance of NTs-WS2@C Nanocomposites for Lithium-Ion and Sodium-Ion Batteries. *ACS Appl. Mater. Interfaces* **2022**, *14* (41), 46386−46400.

(20) Li, Y.; Liang, Y.; Hernandez, F. C. R.; Yoo, H. D.; An, Q.; Yao, Y. Enhancing sodium-ion battery performance with interlayer-expanded MoS2−PEO nanocomposites. *Nano Energy* **2015**, *15*, 453−461.

(21) Ren, X.; Zhao, Q.; McCulloch, W. D.; Wu, Y. MoS2 as a long-life host material for potassium ion intercalation. *Nano Res.* **2017**, *10* (4), 1313−1321.

(22) Dey, S.; Singh, G. Sodium and potassium ion storage in cation substituted 2D MoWSe2: insights into the effects of upper voltage cut-off. *Nanotechnology* **2023**, *34* (38), No. 385401.

(23) Li, J.; Tang, S.; Yuan, Q.; Hao, J.; Li, Z.; Wang, T.; Wang, C.; Pan, L. Dual modification of Ti3C2Tx MXene hybridization and cut-off voltage adjustment for MoS2 to achieve stable sodium storage performance. *Mater. Chem. Front.* **2023**, *7* (5), 917−928.

(24) Ou, X.; Liang, X.; Zheng, F.; Wu, P.; Pan, Q.; Xiong, X.; Yang, C.; Liu, M. In situ X-ray diffraction investigation of CoSe2 anode for Na-ion storage: Effect of cut-off voltage on cycling stability. *Electrochim. Acta* **2017**, *258*, 1387−1396.
(25) Wang, J.; Yang, M.; Wang, J.; Liu, D.; Zou, G.; Liu, B.; Tse, J. S.; Li, L.; Ren, L.; Peng, Q. Lithiation MAX derivative electrodes with low overpotential and long-term cyclability in a wide-temperature range. *Energy Storage Mater.* **2022**, *47*, 611−619.
(26) Dong, Y.; Xu, Y.; Li, W.; Fu, Q.; Wu, M.; Manske, E.; Kröger, J.; Lei, Y. Insights into the Crystallinity of Layer-Structured Transition Metal Dichalcogenides on Potassium Ion Battery Performance: A Case Study of Molybdenum Disulfide. *Small* **2019**, *15* (15), No. 1900497.
(27) Ghosh, S.; Qi, Z.; Wang, H.; Martha, S. K.; Pol, V. G. WS2 anode in Na and K-ion battery: Effect of upper cut-off potential on electrochemical performance. *Electrochim. Acta* **2021**, *383*, No. 138339.
(28) Delmas, C. Sodium and Sodium-Ion Batteries: 50 Years of Research. *Adv. Energy Mater.* **2018**, *8* (17), No. 1703137.
(29) Rajagopalan, R.; Tang, Y.; Ji, X.; Jia, C.; Wang, H. Advancements and Challenges in Potassium Ion Batteries: A Comprehensive Review. *Adv. Funct. Mater.* **2020**, *30* (12), No. 1909486.
(30) Zhang, W.; Lu, J.; Guo, Z. Challenges and future perspectives on sodium and potassium ion batteries for grid-scale energy storage. *Mater. Today* **2021**, *50*, 400−417.
(31) Feldman, Y.; Frey, G. L.; Homyonfer, M.; Lyakhovitskaya, V.; Margulis, L.; Cohen, H.; Hodes, G.; Hutchison, J. L.; Tenne, R. Bulk Synthesis of Inorganic Fullerene-like MS2 (M = Mo, W) from the Respective Trioxides and the Reaction Mechanism. *J. Am. Chem. Soc.* **1996**, *118* (23), 5362−5367.
(32) Azulay, D.; Kopnov, F.; Tenne, R.; Balberg, I.; Millo, O. Observation of current reversal in the scanning tunneling spectra of fullerene-like WS2 nanoparticles. *Nano Lett.* **2006**, *6* (4), 760−764.
(33) Tenne, R.; Margulis, L.; Genut, M.; Hodes, G. Polyhedral and cylindrical structures of tungsten disulphide. *Nature* **1992**, *360* (6403), 444−446.
(34) Joly-Pottuz, L.; Martin, J. M.; Dassenoy, F.; Belin, M.; Montagnac, G.; Reynard, B.; Fleischer, N. Pressure-induced exfoliation of inorganic fullerene-like WS2 particles in a Hertzian contact. *J. Appl. Phys.* **2006**, *99* (2), No. 023524, DOI: 10.1063/1.2165404.
(35) Su, D.; Dou, S.; Wang, G. WS2@graphene nanocomposites as anode materials for Na-ion batteries with enhanced electrochemical performances. *Chem. Commun.* **2014**, *50* (32), 4192−4195.
(36) Wang, Y.; Kong, D.; Shi, W.; Liu, B.; Sim, G. J.; Ge, Q.; Yang, H. Y. Ice Templated Free-Standing Hierarchically WS2/CNT-rGO Aerogel for High-Performance Rechargeable Lithium and Sodium Ion Batteries. *Adv. Energy Mater.* **2016**, *6* (21), No. 1601057.
(37) Zhu, Q.; Li, W.; Wu, J.; Tian, N.; Li, Y.; Yang, J.; Liu, B.; Jiang, J. Vacancy engineering in WS2 nanosheets for enhanced potassium-ion storage. *J. Power Sources* **2022**, *542*, No. 231791.
(38) Geng, S.; Zhou, T.; Jia, M.; Shen, X.; Gao, P.; Tian, S.; Zhou, P.; Liu, B.; Zhou, J.; Zhuo, S.; Li, F. Carbon-coated WS2 nanosheets supported on carbon nanofibers for high-rate potassium-ion capacitors. *Energy Environ. Sci.* **2021**, *14* (5), 3184−3193.
(39) Luo, X.; Huang, J.; Cao, L.; Li, J.; Xu, Z.; Kajiyoshi, K.; Zhao, Y.; Yang, H.; Liu, Y.; Li, Z. Constructing multi-dimensional migration channel by nickel-doped WS2 composite: High speed sodium and potassium ion storage kinetics in WS2 nanosheets. *Chem. Eng. J.* **2023**, *464*, No. 142579.
(40) Wu, Y.; Xu, Y.; Li, Y.; Lyu, P.; Wen, J.; Zhang, C.; Zhou, M.; Fang, Y.; Zhao, H.; Kaiser, U.; Lei, Y. Unexpected intercalation-dominated potassium storage in WS2 as a potassium-ion battery anode. *Nano Res.* **2019**, *12* (12), 2997−3002.
(41) Deng, L.; Zhang, Y.; Wang, R.; Feng, M.; Niu, X.; Tan, L.; Zhu, Y. Influence of KPF6 and KFSI on the Performance of Anode Materials for Potassium-Ion Batteries: A Case Study of MoS2. *ACS Appl. Mater. Interfaces* **2019**, *11* (25), 22449−22456.
(42) Yu, S.; Jung, J.-W.; Kim, I.-D. Single layers of WS2 nanoplates embedded in nitrogen-doped carbon nanofibers as anode materials for lithium-ion batteries. *Nanoscale* **2015**, *7* (28), 11945−11950.
(43) Bhandavat, R.; David, L.; Singh, G. Synthesis of Surface-Functionalized WS2 Nanosheets and Performance as Li-Ion Battery Anodes. *J. Phys. Chem. Lett.* **2012**, *3* (11), 1523−1530.
(44) Lim, Y. V.; Huang, Z. X.; Wang, Y.; Du, F. H.; Zhang, J.; Chen, T. P.; Ang, L. K.; Yang, H. Y. WS2−3D graphene nano-architecture networks for high performance anode materials of lithium ion batteries. *RSC Adv.* **2016**, *6* (109), 107768−107775.
(45) Xu, Y.; Wang, K.; Yao, Z.; Kang, J.; Lam, D.; Yang, D.; Ai, W.; Wolverton, C.; Hersam, M. C.; Huang, Y.; Huang, W.; Dravid, V. P.; Wu, J. In Situ, Atomic-Resolution Observation of Lithiation and Sodiation of WS2 Nanoflakes: Implications for Lithium-Ion and Sodium-Ion Batteries. *Small* **2021**, *17* (24), No. 2100637.
(46) Chen, Y.; Li, L.; Guo, L. Two-Dimensional Metal-Containing Nanomaterials for Battery Anode Applications. *ChemElectroChem* **2020**, *7* (15), 3193−3210.
(47) Zhao, W.; Ma, X. Hierarchical Scalelike Yolk−Shell Construction Assembled via Ultrathin MoSe2 Nanoplates Incorporated into Metal−Organic Frameworks Derived Porous Carbon Spheres as Highly Durable Anode for Enhanced Sodium Storage. *ACS Sustainable Chem. Eng.* **2020**, *8* (51), 19040−19050.
(48) Zhou, J.; Qin, J.; Guo, L.; Zhao, N.; Shi, C.; Liu, E.-z.; He, F.; Ma, L.; Li, J.; He, C. Scalable synthesis of high-quality transition metal dichalcogenide nanosheets and their application as sodium-ion battery anodes. *J. Mater. Chem. A* **2016**, *4* (44), 17370−17380.
(49) Sahoo, R.; Singh, M.; Rao, T. N. A Review on the Current Progress and Challenges of 2D Layered Transition Metal Dichalcogenides as Li/Na-ion Battery Anodes. *ChemElectroChem* **2021**, *8* (13), 2358−2396.
(50) Cook, J. B.; Kim, H.-S.; Lin, T. C.; Lai, C.-H.; Dunn, B.; Tolbert, S. H. Pseudocapacitive Charge Storage in Thick Composite MoS2 Nanocrystal-Based Electrodes. *Adv. Energy Mater.* **2017**, *7* (2), No. 1601283.
(51) Ryu, W.-H.; Wilson, H.; Sohn, S.; Li, J.; Tong, X.; Shaulsky, E.; Schroers, J.; Elimelech, M.; Taylor, A. D. Heterogeneous WSx/WO3 Thorn-Bush Nanofiber Electrodes for Sodium-Ion Batteries. *ACS Nano* **2016**, *10* (3), 3257−3266.
(52) Zeng, F.; Cheng, W.; Pan, Y.; Yu, M.; Qu, Y.; Yuan, C. Monofaceted WO3−x nanorods in situ hybridized in carbon nanosheets for ultra-fast/stable sodium-ion storage. *J. Mater. Chem. A* **2020**, *8* (45), 23919−23929.
(53) Chu, S.; Yu, M.; Liu, B.; Lu, T.; Hou, Z.; Qu, Y.; Zeng, F. WO3-x@W2N heterogeneous nanorods cross-linked in carbon nanosheets for electrochemical potassium storage. *Chem. Eng. J.* **2022**, *435*, No. 135188.
(54) Wang, J.; Polleux, J.; Lim, J.; Dunn, B. Pseudocapacitive Contributions to Electrochemical Energy Storage in TiO2 (Anatase) Nanoparticles. *J. Phys. Chem. C* **2007**, *111* (40), 14925−14931.
(55) Choi, W.; Choudhary, N.; Han, G. H.; Park, J.; Akinwande, D.; Lee, Y. H. Recent development of two-dimensional transition metal dichalcogenides and their applications. *Mater. Today* **2017**, *20* (3), 116−130.
(56) Augustyn, V.; Come, J.; Lowe, M. A.; Kim, J. W.; Taberna, P.-L.; Tolbert, S. H.; Abruña, H. D.; Simon, P.; Dunn, B. High-rate electrochemical energy storage through Li+ intercalation pseudocapacitance. *Nat. Mater.* **2013**, *12* (6), 518−522.
(57) Ghosh, S.; Kiran Kumar, V.; Kumar, S. K.; Biswas, S.; Martha, S. K. An insight of sodium-ion storage, diffusivity into TiO2 nanoparticles and practical realization to sodium-ion full cell. *Electrochim. Acta* **2019**, *316*, 69−78.
(58) Dey, S.; Singh, G. WS2 Nanosheet Loaded Silicon-Oxycarbide Electrode for Sodium and Potassium Batteries. *Nanomaterials* **2022**, *12* (23), No. 4185, DOI: 10.3390/nano12234185.
(59) Dey, S.; Mujib, S. B.; Singh, G. Enhanced Li-Ion Rate Capability and Stable Efficiency Enabled by MoSe2 Nanosheets in Polymer-Derived Silicon Oxycarbide Fiber Electrodes. *Nanomaterials* **2022**, *12* (3), No. 553, DOI: 10.3390/nano12030553.

https://doi.org/10.1021/acsomega.3c09758
ACS Omega 2024, 9, 17125−17136

(60) Li, Z.; Deng, L.; Kinloch, I. A.; Young, R. J. Raman spectroscopy of carbon materials and their composites: Graphene, nanotubes and fibres. *Prog. Mater. Sci.* **2023**, *135*, No. 101089.
(61) Santato, C.; Odziemkowski, M.; Ulmann, M.; Augustynski, J. Crystallographically Oriented Mesoporous WO3 Films: Synthesis, Characterization, and Applications. *J. Am. Chem. Soc.* **2001**, *123* (43), 10639−10649.

NOTE ADDED AFTER ASAP PUBLICATION

Due to a production error, this paper was published ASAP on Apri l, 2024 with the wrong Supporting Information file. The corrected version was reposted on April 2, 2024.

https://doi.org/10.1021/acsomega.3c09758
ACS Omega 2024, 9, 17125−17136